Computer Methods in Biomechanics and Biomedical Engineering,
Vol. 8, No. 4, August 2005, 229–240

Taylor & Francis
Taylor & Francis Group

Three-dimensional analysis for radio-frequency ablation of liver tumor with blood perfusion effect

TONY W. H. SHEU†*, C. W. CHOU†, S. F. TSAI‡ and P. C. LIANG¶

†Department of Engineering Science and Ocean Engineering, National Taiwan University, No. 1, Sec. 4, Roosevelt Road, Taipei, Taiwan 106, Republic of China
‡Department of Marine Engineering, National Taiwan Ocean University, Taiwan
¶Department of Medical Imaging, National Taiwan University Hospital, Taiwan

(Received 24 May 2005)

Increase of temperature above 50 $\sim$ 60°*C* for few minutes by the emitted radio-frequency (RF) energy has been shown to be able to denaturate the intracellular proteins and destruct membranes of tumor cells. To improve the efficacy of this thermal therapy, it is important to investigate factors that may affect the RF heating characteristics for the hepatocellular carcinoma and metastatic liver tumors. In order to make sure the applied RF energy is adequate to ablate the target tumor, a 3D thermoelectric analysis for the system consisting of liver, liver arteries and 4 mm diameter tumor is conducted. The effect of blood perfusion is addressed in this study.

Keywords: Radio-frequency; Hepatocellular carcinoma; Thermoelectric analysis; Blood perfusion

1. Introduction

Human liver has functions in secreting bile, storing glycogen, distributing nutrients from the blood and gastrointestinal tract, and eliminating endogenous/exogenous substrates and toxins. This functionally complex and important organ is unfortunately susceptible to primary and metastatic malignant diseases (McGaham *et al.* 1992). In Taiwan, more than 7000 patients per year suffer from primary hepatocellular carcinoma (HCC) and metastatic colorectal liver carcinoma. HCC, in the majority of cases (or 80%), originates from liver cirrhosis (The Liver Cancer Study Group of Japan 1987). Statistically, liver cancer is now the second leading cause of death (Huang *et al.* 2001). Over one million patients were also reported to die of primary and metastatic malignancies worldwide (Curley *et al.* 1999).

Surgical resection of primary and metastatic hepatic tumors remains the gold standard of therapy (Steele and Ravikumar 1989). To avoid further destruction and deterioration of liver function, surgical treatment is not recommended. Moreover, some patients may not be suitable for surgical resection due to multifocal disease, tumor size, tumor location or coagulopathies (Tungjitkusolmun *et al.* 2002). Thus, non-surgical interventions such as hepatic artery infusion chemotherapy, percutaneous ethanol injection (PEI), cryotherapy, microwave coagulation therapy (MCT) and laser induced thermotherapy (LITT) have been developed (Huang *et al.* 2001, Lin and Lin 2003). These therapies may produce adverse side effects and none of them have yet been demonstrated as the long-term survival treatment. Rapid ablation of large volume tissue is also possible by thermal energy generated by the high-frequency radio-frequency (RF). This thermoablative therapy requires accurate positioning of the tumor, in addition to effectively heating and coagulating the target tissue.

With an ever-improving image technologies, RF ablation (RFA) aided with the percutaneous image-guided CT, ultrasound and MRI is now accepted as a promising minimally invasive means. It is particularly recommended for patients not eligible for surgical cure of hepatic malignancies without losing their entire segments or lobes of normal liver (McGaham *et al.* 1990, Curley *et al.* 2000). The most frequently employed focal ablative techniques are cryoablation and RF ablation. While the post-treatment recurrence rate of cryoablation is known to be lower than RF, an open surgery is generally necessary

*Corresponding author. E-mail: twhsheu@ntu.edu.tw

Computer Methods in Biomechanics and Biomedical Engineering
ISSN 1025-5842 print/ISSN 1476-8259 online © 2005 Taylor & Francis
http://www.tandf.co.uk/journals
DOI: 10.1080/10255840500289731

because of the probe size and the risk of bleeding (Tungjitkusolmun *et al.* 2002). In contrast, the RF ablation therapy is safe and can be applied percutaneously owing to the increasingly smaller needle probes designed for RF ablation.

Although RF ablation has gained wide acceptance as a minimally invasive means to avoid open laparotomy, it has the problem with higher recurrence rate than hepatic resection. Thermal therapy of tumors near the large portal triad needs special attention because of the possibility of damaging bile duct, in addition to bringing much pain to patients within 24 h. Ablation of tumors adjacent to the diaphragm, liver capsule, gall bladder and large blood vessels also encounters risks of different kinds mentioned in the excellent review paper (Huang *et al.* 2001). Clinically, patients can not bear the placement of RF probes twice in the same day. Radio-frequency ablation becomes technically challenging for patients having tumors have more than one or their sizes are too large to be completely ablative at the first time. Therefore, there is a demand for simulation tools to accurately and efficiently ablate tumors without over-heating the tissues in close proximity to the RF probe and ablating the healthy tissues. It is best hoped that surgeons can avoid this therapy again.

During the RFA therapy, RF energy is radiated from electrodes into the adjacent tissues. The conduction heat emitted from liver tissues is known to be proportional to the square of the RF alternating current (AC), which decreases also proportionally with the square of the distance from the electrode. The resistive heat from the ablation electrode will, thus, be decreased with the distance to the fourth power (Lorentzen 1996). This underlying theory explains why the tissue temperature can be decreased rapidly with the increasing distance measured from the electrode. Besides the dissipative nature of the RF heat in tissues, some other issues need to be taken into account. Amongst the important factors, we need to take capillaries and large blood vessels into account since blood flow can take away the thermal energy heat which deposites on the hepatic tumor cells. According to the works in (Rosenthal *et al.* 1992, Goldberg *et al.* 1995, Gazelle *et al.* 2000), an increase of temperature by additional eight degree may be needed to produce the same coagulation *in vivo* due to tissue perfusion. Thus, tissue perfusion effect should be taken into account during the hepatic RFA therapy (Huang *et al.* 2001, Arkin *et al.* 1994).

The rest of the paper is organized as follows. In Section 2 we briefly describe the RFA system. Section 3 is devoted to formulate the thermoelectric system. The bioheat equation which can theoretically describe the transfer of heat in liver tissues and the working equations for blood flow in liver arteries are detailed. This is followed by a brief description of the employed finite volume method for the discretization of conservation equations. Boundary conditions for the electric and hemodynamic field equations are also given in the same section. In Section 5 the results for cases with/without considering blood perfusion are presented and discussed in detail. Finally, we conclude with few remarks in Section 6.

2. RFA therapy

The closed-loop circuit in a RFA system consists of needle electrodes, tissues and grounding pads on the thighs or legs. The electrode shaft is made of a metal that is insulated except for the exposed conductive tip. An alternating current, in the frequency range from 460 to 500kHz, flowing from the uninsulated needle tip to the grounding pads creates a voltage or electric field. This applied alternating current can generate ionic agitation and create localised heating. The resultant frictional heating of tissues surrounding the electrode generates localised areas of coagulative necrosis and tissue desiccation. Denaturation of intercellular proteins and destruction of cell membranes are known to be the direct consequences of heating liver cells to a temperature above $45 \sim 60^{\circ}$C (Lin and Lin 2003).

Three RFA needle electrodes have been approved by US Federal Drug Administration (FDA), namely, the cluster electrode Radionics (Radionics Inc. Burlington MA) (Radionics, Cool-Tip RF Ablation 2002), Rita expandable needle (Mountain View CA) (Rita Medical Systems, Starburst XL needle 2002), and Le Veen needle (Radiotherapeutics, Mountain View CA) (RadioTherapeutics, Radiofrequency Ablation System 2002). The Rita RF electrode of model-30 (Tungjitkusolmun *et al.* 2002), schematic in figure 1, is chosen for the current study. The investigated 15-gauge probe could be fully deployed (30 mm diameter) and was inserted deep in the middle of the tumor. The 10 mm distal section of the stainless-steel trocar is subject to alternating current while the remaining parts are insulated. We combined the liver model schematic in figure 2 and the liver artery model shown in figure 3 to construct the CAD model schematic in figure 4. The effect of blood perfusion is investigated by performing the three-dimensional analysis subject to the specified convective heat transfer coefficient on the vessel wall. More logically, the same perfusion problem can be analyzed differently by solving the time-dependent incompressible Navier-Stokes equations for blood in vessels together with the equations for the thermoelectric system. All calculations were performed on a Pentium-4 CPU PC with 1.0 GB of RAM and 80 GB of hard disk space.

3. Working equations for the thermoelectric system

The alternating current emitted from the inserted electrode can agitate ions and in turn can generate the frictional heat. The resulting locally deposited heat can be radiated outwards by conduction mode to heat the adjacent tissues. Due to tissue conductivity, liver temperature can decrease rapidly with the distance from the electrode to the fourth

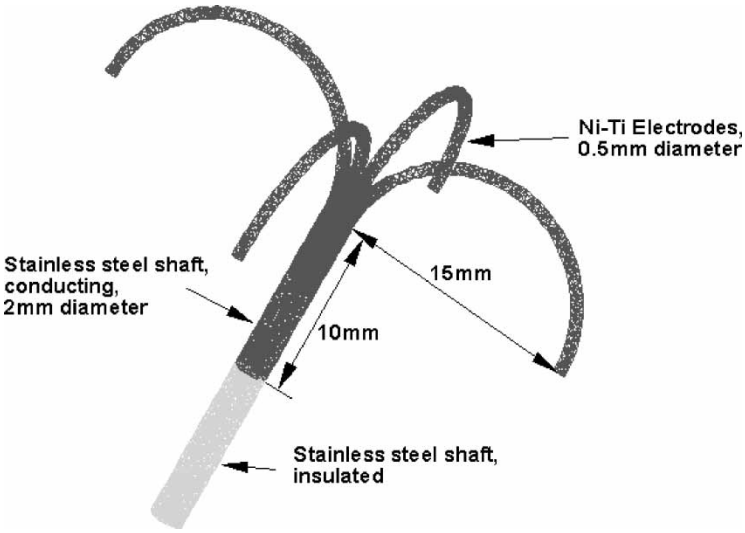

Figure 1. Schematic of the Rita probe for the current hepatic ablation study.

power (Lorentzen 1996). In addition, the tissue impedance can yield a sharply decreased lesion current (Nath *et al.* 1994) and, in many cases, heating of tissues will be terminated near the electrode. Note that the tumor cells adjacent to the large blood vessels are more difficult to be adequately ablated because blood flow can take away the applied heat in its adjacent tumor. Taking into account the above mentioned limitations to the RFA therapy, a theoretical heat transfer study becomes essential to accurately predict the energy deposition. The ultimate goal is to maximize the ablation zone within a shorter treatment time.

For modeling the heat sink effect, the derived working equation for heat transfer in liver tissues is as follows (Haemmerich *et al.* 2001; Chang 2003; Ebbini *et al.* 1998)

$$\rho c \frac{\partial T}{\partial t} = \nabla \cdot (k \nabla T) + \vec{J} \cdot \vec{E} - h_{\mathrm{bl}}(T - T_{\mathrm{bl}}) - Q_m \qquad (1)$$

The above bioheat equation involves the energy $Qm(W/m^3)$ generated in the metabolic processes. This amount of heat is negligibly small in comparison to the other three energies (Tungjitkusolmun *et al.* 2002). Material properties used in the derivation of bioheat equation include the medium density $\rho(kg/m^3)$, specific heat $c(J/kg{\cdot}K)$, and the thermal conductivity $k(W/m{\cdot}K)$. The above bioheat equation for solving the temperature $T(K)$ has a close link with the electric field through

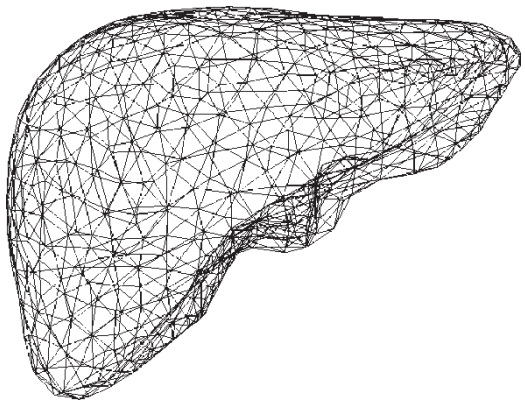

Figure 2. The generated surface meshes for the liver under current investigation.

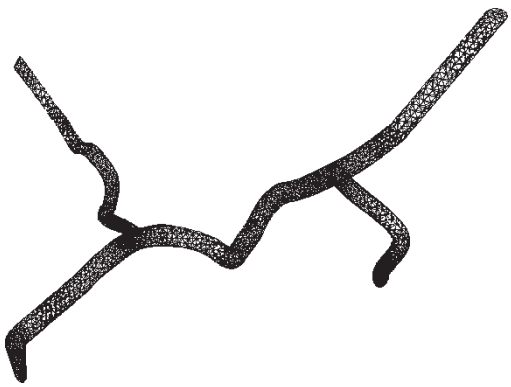

Figure 3. The generated surface meshes for the investigated liver artery.

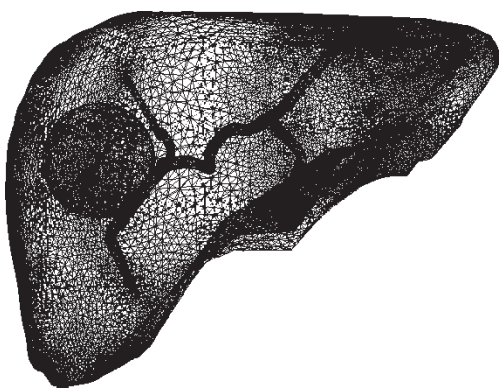

Figure 4. Schematic of the CAD model for the ablation with liver artery.

the current density $J(A/m^2)$ and electric field intensity $E(V/m)$. The coupling of equation (1) with the hemodynamic equations for blood flow is by way of the inegligible convective heat transfer in the arterial blood vessel.

The first term on the right hand side of equation (1) accounts for heat conduction in the solid medium while the second term is called the Joule heat. Since equation (1) must be solved in conjunction with the electrical field equation for $\vec{J}\cdot\vec{E}$, we need to solve the electric current continuity equation to calculate the Joule heat $\vec{J}\cdot\vec{E}$. The third term on the right hand side represents the heat loss to blood perfusion. The thermoelectric system should be further coupled with the flowfield for calculating the heat transfer coefficient $h_{\rm bl}$ by virtue of $k(\partial T/\partial n) = h_{\rm bl}(T - T_{\rm bl})$, where $T_{\rm bl}$ denotes the blood temperature. One may prescribe $h_{\rm bl}(\mathrm{W/m^3\,K})$ by experience on the vessel wall by $h_{\rm bl} = \rho_{\rm bl}\cdot c_{\rm bl}\cdot w_{\rm bl}$, where $\rho_{\rm bl}(\mathrm{kg}/m^3)$ is blood density, $c_{\rm bl}(J/kg\,K)$ is blood specific heat and $w_{\rm bl}(1/s)$ is blood perfusion. A more logical way of analyzing this problem is to solve the Navier-Stokes equations for blood flow in the vessel. Therefore, both ways will be considered to study the tissue perfusion effect. The simulated difference obtained from the above-mentioned two ways will be addressed.

As said earlier, we need to consider the following electric current continuity equation, namely, $(\partial\rho_e/\partial t) + \nabla\cdot\vec{J}_e = 0$ for the currently investigated thermoelectric system. Here, J_e is the electric current density (A/m^2) and $\rho_e(C/m^3)$ is the charge density. Substitution ρ_e from Gauss' law ($\nabla\cdot\vec{D} = \rho$, where $\vec{D}$ is the electric displacement and $\rho_e(C/m^3)$ is the charge density) for electricity into the continuity equation for charge, we are led to have $\nabla\cdot[\vec{J} + (\partial\vec{D}/\partial t)] = 0$. Assuming that the total current density $\vec{J}$ results solely from the conduction current (e.g., $\vec{J} = \vec{J}_c = \sigma\vec{E}$, where σ is the electrical conductivity $(\Omega - m)^{-1}$), the charge equation for an isotropic linear dielectric (e.g., $\vec{D} = \varepsilon\vec{E}$, where ε is known as the permittivity) becomes

$$\nabla\cdot\left[\sigma\vec{E} + \frac{\partial\varepsilon\vec{E}}{\partial t}\right] = 0 \tag{2}$$

Note that the electrical resistivity $1/\sigma$ is a specified constant. Also, it can be varied with T according to $\sigma = \sigma_0[1/1 + \alpha(T - T_0)]$, where σ_0 is the electrical conductance at T_0 and α is the coefficient of resistivity.

The electric field can be expressed in terms of electric potential ϕ and magnetic vector potential $\vec{A}$, implying that $\vec{E} = -\nabla\phi - (\partial\vec{A}/\partial t)$. By employing the time-independent magnetic field assumption (i.e., $\partial\vec{A}/\partial t = 0$), the resulting equation $\vec{E} = -\nabla\phi$ is substituted into equation (2) to derive the field equation for the electric potential ϕ as

$$\nabla\cdot\left[\sigma\nabla\phi + \varepsilon\frac{\partial\nabla\phi}{\partial t}\right] = 0 \tag{3}$$

Note that equations (1) and (3) constitute the thermoelectric differential system. After solving the equation for ϕ, we can calculate the Joule heat from $\vec{J}\cdot\vec{E} = \sigma|\vec{E}|^2 = \sigma(\nabla\phi)^2$.

To rigorously determine the convective heat transfer coefficient shown in the bioheat equation, the following dimensionless incompressible Navier-Stokes, continuity, and energy equations must be taken in account:

$$\frac{\partial u_i}{\partial t} + \frac{\partial(u_m u_i)}{\partial x_m} = -\frac{\partial p}{\partial x_i} + \frac{1}{\mathrm{Re}}\frac{\partial^2 u_i}{\partial x_m \partial x_m} \tag{4}$$

$$\frac{\partial u_i}{\partial x_i} = 0 \tag{5}$$

$$\frac{\partial(\rho h_0)}{\partial t} + \nabla\cdot(\rho\vec{V}h_0) = \frac{\partial p}{\partial t} + \nabla\cdot(k\nabla T) + \frac{\partial(u_m\tau_{nm})}{\partial x_n} + S_h \tag{6}$$

In the above, u_i $(i = 1 \sim 3)$ is the velocity component along the i-direction, p the hydrodynamic pressure, τ_{nm} is the shear stress tensor, The subscripts m and n seen above denote the summation from 1 to 3 (i.e., $\sum_{n,m=1}^{3}\tau_{nm}$). S_h stands for the possibly present sources due to reaction, radiation, spray, and body force, etc. h_o is known as the total enthalpy, which is defined as $h_0 = i_e + (p/p) + (1/2)(u^2 + v^2 + w^2)$, i_e the internal energy, Field variables u, v and w denote the velocity of blood in i, j, k directions, respectively, and Re is the Reynolds number.

4. Numerical method

The outer surface of the currently investigated liver is assumed to have the same temperature as the human body temperature 37°C. Voltages ranging from 15 to 30 V are applied at the Ni–Ti electrode and 10 mm distal section of the stainless-steel trocar. Both electrode and trocar are thermally non-conducting while the shaft is thermally and electrically non-conducting. On the vessel wall, we specify $h_{\rm bl} = \rho_{\rm bl}\cdot c_{\rm bl}\cdot w_{\rm bl}$ as the thermal boundary condition. For the sake of comparsion, we also solve for the incompressible Navier-Stokes equations for the hemodynamic variables to obtain $h_{\rm bl}$. This approach can preserve energy balance at the interface of blood and liver artery vessel. As usual, we prescribe zero velocity boundary condition on the vessel wall.

The interface between blood and liver is assumed to be thin. To avoid the need to cluster grid points in between the blood vessel and liver tissues, we describe below the method applied at the thin wall schematic in figure 5, which shows two arbitrarily chosen neighboring cells that are separated by a thin wall. A_1, A_2 and A represent three different materials, namely, tissues, blood and vessel wall (thin wall), respectively. Denote K_1, K_2 and K as the conductivities of cell-1, cell-2 and the thin-wall, and δ_1, δ_2 and δ as the cell-center to face-center distance at cell-1,

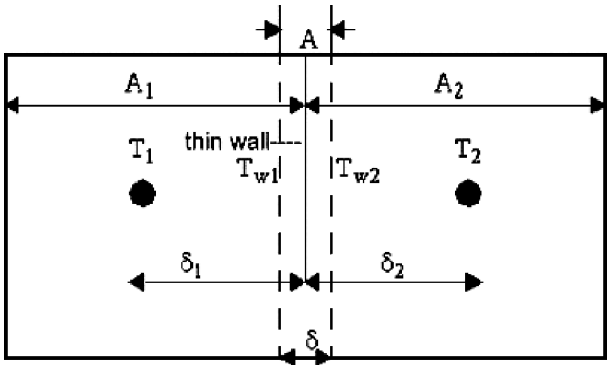

Figure 5. Schematic of the stencil points near the interface.

Table 1. Representation of ϕ, ρ, Γ and S shown in equation (11) for different working equations.

	ρ	ϕ	Γ	S
Continuity equation	ρ	1	0	0
Momentum equation	ρ	$\vec{u}$	μ	$-\nabla P$
Laplace's equation	0	ϕ	0	0
Poisson's equation	0	ϕ	0	Constant
Electric current continuity equation	ρ_e	1	0	0

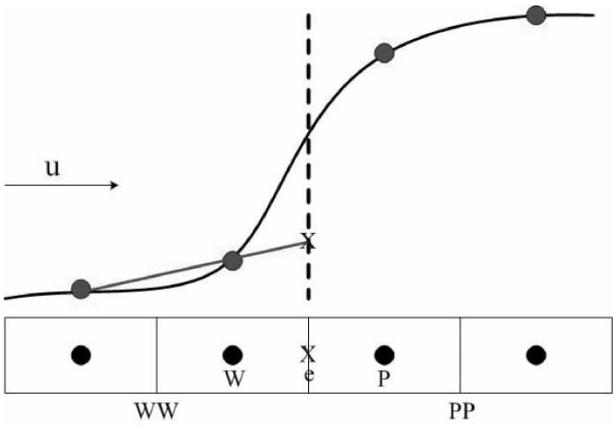

Figure 6. Schematic of the second order upwind scheme.

cell-2 and the thickness of the thin-wall. T_1, T_2 are denoted as the cell-center temperature at cell-1 and cell-2. T_{w1} is the interface temperature of the thin-wall on the cell-1 side and T_{w2}, the cell-2 side. By theory, the heat flux across the

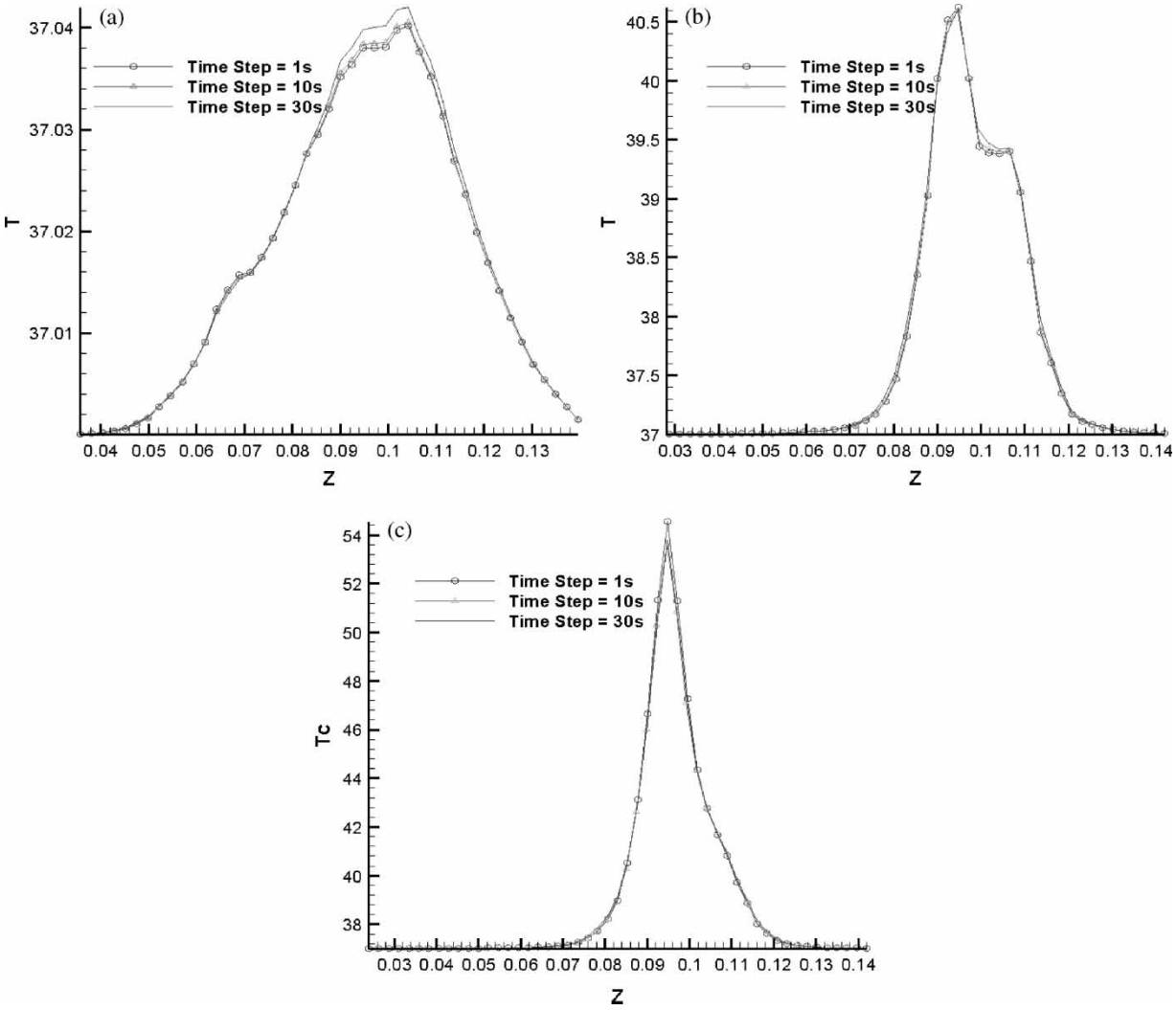

Figure 7. Comparison of temperature profiles at three different cutting planes in the current simulation using three different time steps (1, 10, and 30 s).

thin-wall is continuous, implying that

$$\frac{K_1}{\delta_1}(T_1 - T_{w1}) = \frac{K}{\delta}(T_{w1} - T_{w2}) = \frac{K_2}{\delta_2}(T_{w2} - T_2) = q_w \tag{7}$$

From the above equation, we can obtain

$$T_{w1} = T_1 + \frac{\frac{\delta_1}{K_1}}{\frac{\delta_1}{K_1} + \frac{\delta_2}{K_2} + \frac{\delta}{K}}(T_2 - T_1) \tag{8}$$

and

$$T_{w2} = T_2 + \frac{\frac{\delta_2}{K_2}}{\frac{\delta_1}{K_1} + \frac{\delta_2}{K_2} + \frac{\delta}{K}}(T_1 - T_2) \tag{9}$$

Define K_{eff} as the effective conductivity according to $q_w = (K_{eff}/\delta_1 + \delta_2)(T_1 - T_2)$, the expression for K_{eff} can be derived from equations (7)–(9) as

$$K_{eff} = \frac{\delta_1 + \delta_2}{\frac{\delta_1}{K_1} + \frac{\delta_2}{K_2} + \frac{\delta}{K}} \tag{10}$$

With the above effective conductivity for directly relating the heat flux with the cell-center temperature, the contact resistance boundary can be treated as an interior cell face.

The equations for the coupled hemodynamic and thermoelectric fields can be expressed by the following generalized equation for ϕ:

$$\frac{\partial p\phi}{\partial t} + \nabla \cdot (\rho \vec{V} \phi) = \nabla \cdot (\Gamma \nabla \phi) + S_\phi \tag{11}$$

All variables and coefficients for the equations under current investigation are tabulated in table 1. The solution domain is divided into a finite number of control volumes. Within the cell-centered analysis framework, each working equation is integrated over its computational cell to derive the corresponding finite volume equation. The scheme employed in this article is to evaluate the cell face value using linear interpolation values at two upstream cells, instead of one. The second-order upwind scheme can be written as

$$\phi_e = \begin{cases} \frac{3}{2}\phi_W - \frac{1}{2}\phi_{WW} & if \quad u > 0 \\ \frac{3}{2}\phi_P - \frac{1}{2}\phi_{PP} & if \quad u < 0 \end{cases} \tag{12}$$

where u is the velocity field. Other notations are schematic in figure 6.

Algebraic MultiGrid (AMG) solver is employed in this simulation. The reasons of offering two major advantages over other iterative methods are two folds: (a) the CPU time increases in proportion to the number of unknowns in the equations; (b) faster convergence, in particular, for the case with fully-unstructured meshes. The idea of a multigrid solver is to use a hierarchy of grids, from fine to coarse, to solve a set of equations, with each grid being particularly effective for eliminating errors of wavelength characteristic of the mesh spacing on that grid. The solution method can be best illustrated for a two-grid system. On the fine grid (original grid), residuals are obtained after performing less number of iterations. One then perform iterations on the coarse grid to obtain corrections, with the fine-grid residual being imposed as a source term. This is followed by interpolating the corrections to the fine grid and updating the fine grid solution. The entire procedures are than respeated until the residual is reduced to the desired level.

The solution algorithm for the three-field coupling equations is shown as follows:

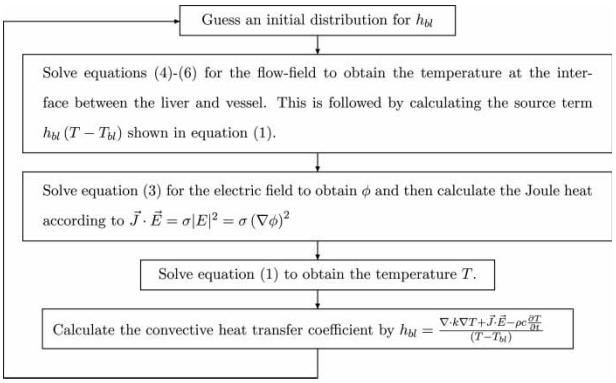

The convergence tolerance chosen in the present calculations was 10^{-5}. The time steps used in the present analysis were 1, 10, and 30 s. Comparison between the three time-step results is shown in figure 7, from which it is observed that there is not much difference. Hence in the present calculations, 30 s time step was used.

5. Results and discussion

In the current simulation, results are obtained for the material properties tabulated in table 2. As figure 8 shows, the simulated temperatures based on the employed two methods are extremely similar. At close scrutiny, the locations where temperature profiles differ most are observed in regions near the blood vessel (such as at $z = 0.08 \sim 0.1$). Moreover, the simulated difference between the two curves led us to know that the convective heat transfer coefficient varies along the vessel wall. Although the simulated difference in temperatures at the chosen line schematic in figure 9 is negligibly small, it does not imply that the method of directly assigning the convective heat transfer coefficient is logical to model the perfusion effect. We inferred, therefore, that the convective heat transfer coefficient is not critical to yield a large difference between the two employed methods. In order to justify this finding, three different h_{bl} are prescribed on the vessel wall and we plot their respective solutions at $x = 0.05$, $y = 0.14$. Figure 10 shows that the simulated

Table 2. Material properties used in the current RFA simulation study.

Simulation region	Material	ρ(kg/m^3)	c(J/kg K)	k(W/m K)	σ(S/m)
Electrode	Ni–Ti	6450	840	18	1×10^8
Trocar	Stainless steel	21500	132	71	4×10^6
Tissue	Liver	1060	3600	0.512	0.333
Tumor	Liver Tumor	999	4200	0.552	0.1168
Liver artery	Blood	1050	4180	0.543	0.667

temperature distributions at $h_{\text{bl}} = 26752$ and 13000 are almost the same. When h_{bl} was reduced to 260, the difference became larger, but its solution was still similar to those simulated at $h_{\text{bl}} = 26752$ and 13000. As we inferred, the temperature distributions are not very sensitive to the convective heat transfer coefficient.

The averaged surface temperature plotted on the tumor surface was chosen to represent the temperature increase in

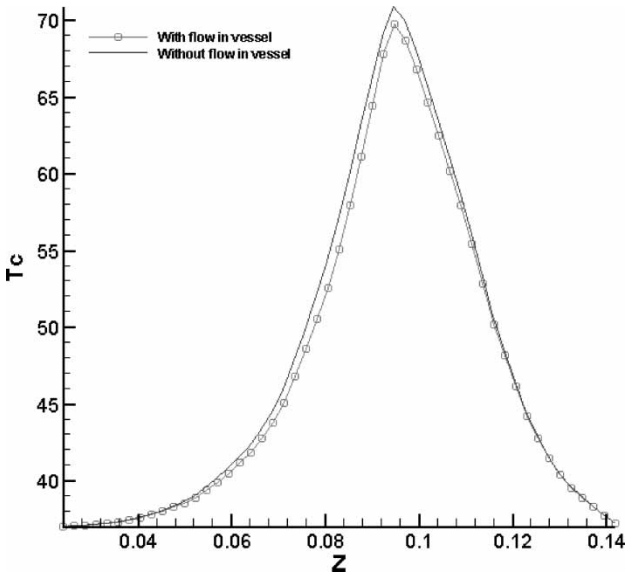

Figure 8. The simulated temperature profile along $y = 0.16$ schematic in figure 7. The circular symbols represent the simulated temperatures by solving the Navier-Stokes equations inside the blood vessel while the curve without the symbols represent the simulated temperatures obtained by assigning the convection heat transfer coefficient on the vessel wall.

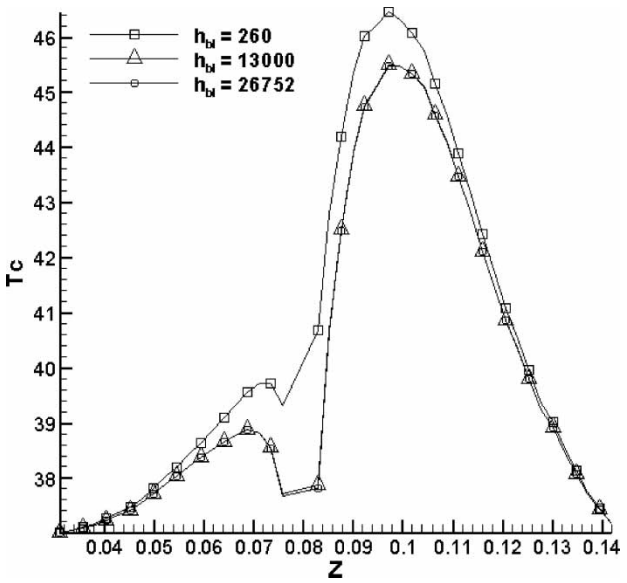

Figure 10. The simulated temperature profiles based on the prescribed values of h_{bl} on the vessel wall along $x = 0.05$ and $y = 0.14$.

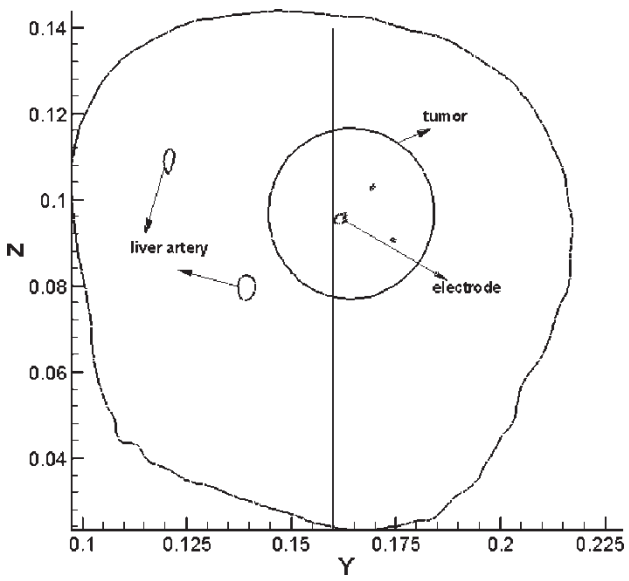

Figure 9. Schematic of the yz-plane at $x = 0.05$.

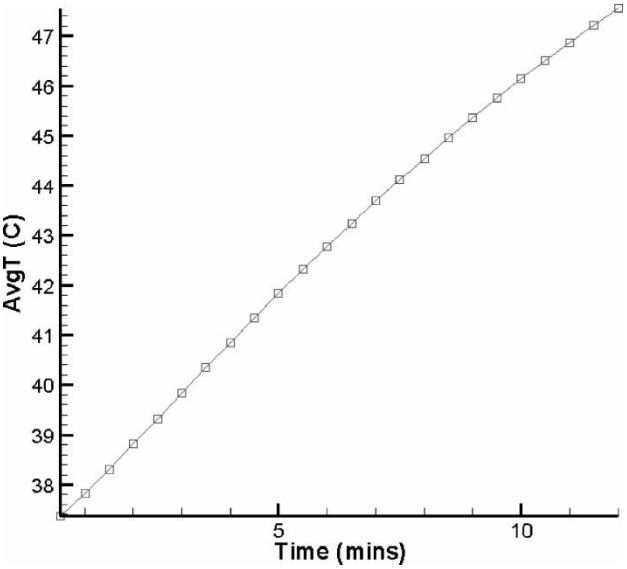

Figure 11. The simulated time-evolving average temperatures on the tumor surface.

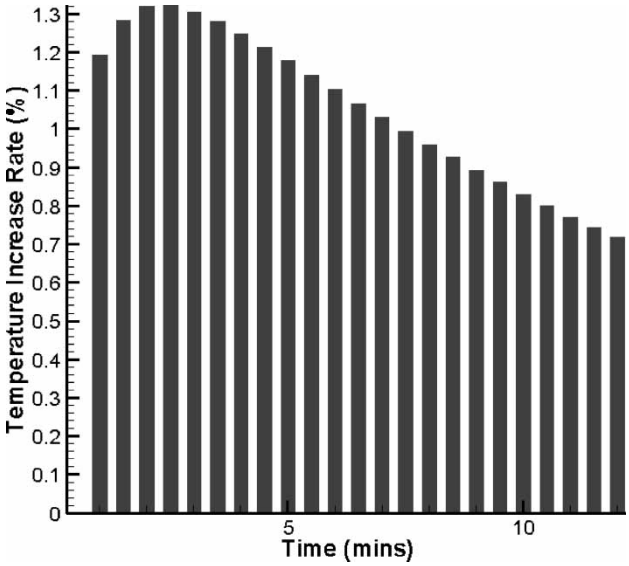

Figure 12. The simulated time evolving averaged rates of temperature increase on the tumor surface for every 30 s.

accordance with the RF-ablation processing time. The temperature increased quite linearly, as shown in figure 11, in the beginning ablation period. In figure 12, the temperature increase is apparent but it gradually takes a dive after 2.5 min.

Conduction and convection heat transfers are two main factors that may affect the temperature distribution at the tumor surface. In the beginning 2.5 min, the temperature has not been raised sufficiently high to cause a noticeable convection heat transfer to occur and conduction remains as the dominant heat transfer mode in this period. After 2.5 min, the convection heat transfer becomes apparent and can take away heat. As a result, the temperature increases slowly but its rate becomes descending. While convection heat transfer increasingly plays its role in this period, the temperature remains dominated by the

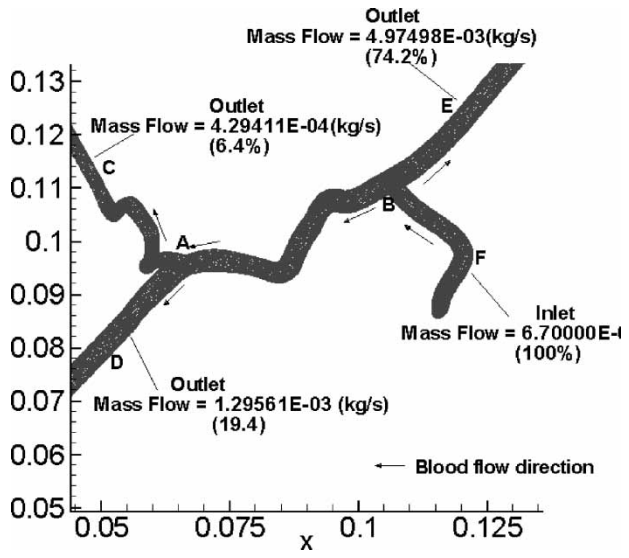

Figure 13. Schematic of the *xz*-plane of the 3D liver artery model and the simulated percentages of mass flow at each branch of the liver artery.

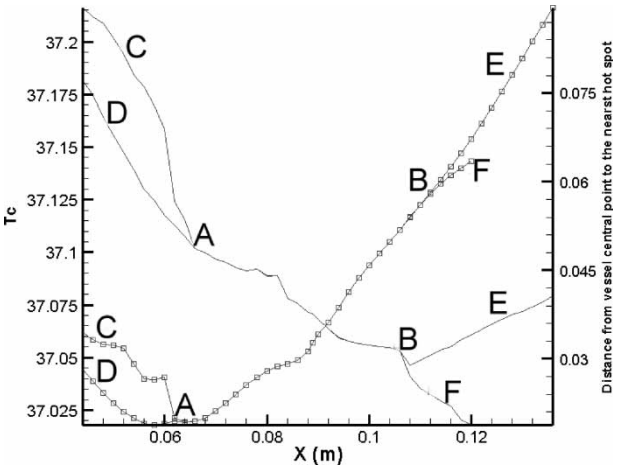

Figure 14. The simulated central temperatures of the liver artery (the lines without symbols) against the distance from the center of the vessel cross section to the nearest hot spot (the lines with symbols).

conduction mode. The reason is that the convection mode is less important in comparison with the conduction mode. This explains why the temperature will be gradually increased.

The blood temperature at the centroid of liver artery varies with the distance from the hot spots, mass flow in each vessel branch, blood vessel curvature and location. In general, the shorter the distance in between the hot spot and vessel, the higher the temperature. The nearest hot spot at the centroid of each cross section is taken into consideration to explain how the hot spot can affect the temperature. Figure 13 is plotted to show that the distance isn't the only factor needed to be taken into consideration. The mass flow, blood vessel location and curvature are also crucial to affect the temperature change inside the liver artery. In view of figure 14, it can be found that though all points along DA and CA are further away from the hot spot than the point A, the temperature is surprisingly lower at point A.

In figure 13, the simulated mass flows along DA and CA branches are smaller than that along AB. The slowly accumulated heats along DA and CA result in higher temperatures than that along AB. The same theory can be applied to reveal why the temperature at each point along CA is higher than the temperatures along DA. Given that the blood flow remains steady, the temperature should

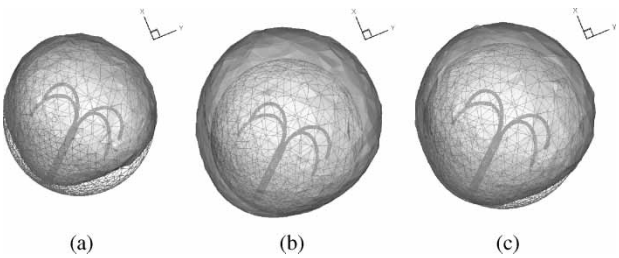

Figure 15. The simulated 50°C iso-surfaces from the RF-ablation solutions at (a) 20 V AC power applied on the electrode; (b) 25 V AC power applied on the electrode; (c) 22.5 V AC power on the electrode.

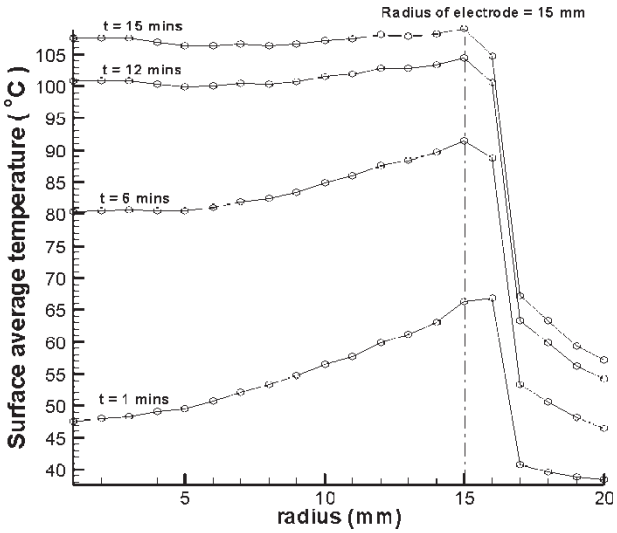

Figure 16. The simulated time varying averaged surface temperatures at different radius of the tumor.

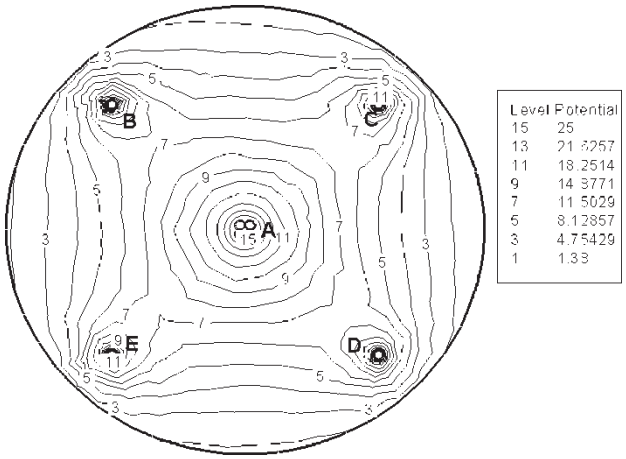

Figure 17. The simulated electric potential contours at a cross section passing through four pinnacles of the electrode.

vary inversely with the distance. This is not the case in the sense that the blood vessel location must be taken into account. Along CA, the heat is sent downstream and propagates towards C, which is also affected by the heat source. Subject to the above mentioned two influences, there is no wonder why the temperature at C is higher than that at A. The same can be applied to the relations between D and A, B and E. Another interesting thing worthy to point out is that the temperature does not rise or descend smoothly along AB. As figure 14 shows, there is a protrusion occurring in the midway. This protruded location has a larger curvature and, thus, can incur slow blood flow, thereby inducing heat to clog at that location.

As we know, if the lesion size is not sufficiently large (figure 15(a)) to cover the whole tumor, the recurrence rate for the themoablative therapy of cancer will be high. If the lesion size is too large (figure 15(b)), the over-heating will destruct some healthy tissues and can cause great pain to the patient. To avoid improper thermoablative therapy, the current simulation can be a scientific means to pre-estimate the preferable location of the electrode, proper applied voltage within the allowable surgery time. The tumor can then be destroyed within the shortest therapy duration without causing serious damage to the healthy tissues (figure 15(c)).

Figure 16 shows that the temperature at a location near the radius $= 15\,mm$ is seen to have a higher magnitude than those at the other radius in the beginning ablation period. Afterwards, the temperature inside the volume of radius $= 15\,mm$ is evolved to be uniform while the temperature outside the volume of radius $= 15\,mm$ is still low. In figure 17, there are five hot spots (A $\sim$ E), at which the electric potential (four deployed electrodes and the central of the main electrode body) can be conveyed to the tumor. Because the sectional area of the hot spot A is larger than the other four hot spots, the electric potential near A is distributed more uniformly than those near the other four hot spots. Thus, the temperature at A is lower than those at the other four hot spots because Joule heat is created by the electric potential difference. Even though, the temperature at A is still higher than those at the other locations at this cross section excluding the four hot spots we have

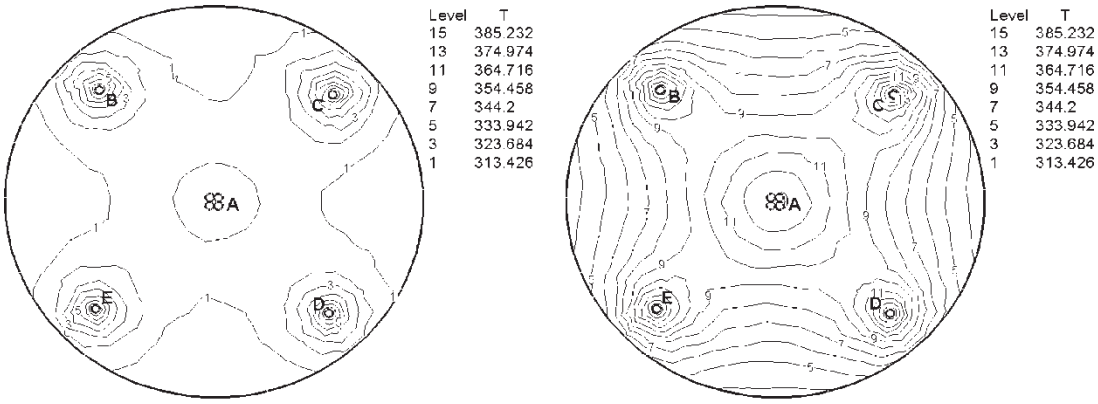

Figure 18. (a) The simulated temperature contours at a cross section passing through the four pinnacles of the electrode at $t = 1$ min. (b) The simulated temperature contours at a cross section passing through four pinnacles of the electrode at $t = 12$ min.

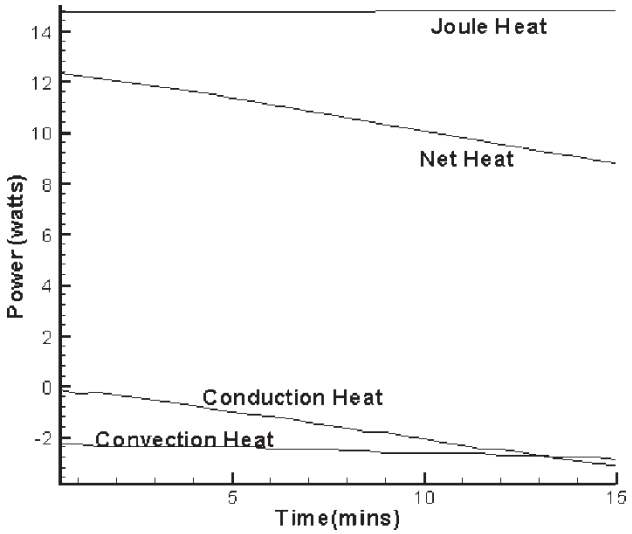

Figure 19. Plots of the simulated heats of different sorts against time for the case considered at 25 V.

mentioned before. Figure 18 clearly shows these five hot spots at the cross section. As figure 16 shows, the temperature distribution inside the tumor is not uniformly distributed in the first minute, The temperature outside 15 *mm* is mainly controlled by the Fourier's law of heat conduction. As time goes by, the range between the five hot spots becomes increasingly uniform as shown in figure 16.

In the RF ablation operation, there are four main heat sources that need to be considered. The first heat source is called the Joule heat, which provides the ablative energy deposition. The second and third ones are conduction heat and convection heat which are essential because they may take away the heat needed to destroy the tumor. We are prompted to know which will affect the operation more because all of them change with time. Figure 19 shows that the convection heat takes away more heat in the beginning period. As time goes by, the conduction heat increases in amount and surpasses the convection heat. To know exactly when one will surpass the other, it is important to estimate two kinds of heat carefully in this operation. The net heat is determined by subtracting the conduction and convection heats (form the Joule heat).

Figure 20 shows the over-heating volume at which the temperature is above $50°C$ in the tumor. The heat deposited inside the tumor can be conducted outwards and transferred to the normal liver tissues, the conduction mode plays a crucial role here. The line with symbols represents the $50°C$ lesion volume which includes the volume of tumor and liver, and the line without symbols represents the $50°C$ lesion volume which contains only the tumor. The bar represents the difference between the volumes with and without symbols. The resulting over-heating volume may make patients feel uncomfortable or can even cause some dangerous effects. Figures 21 (a), (b) and (c) are the plots, similar to figure 20, simulated for the $45°C$ lesion volume at the applied voltages with 20 V, 22.5 V, and 25 V. Because of the different applied voltages, the time needed to cause the whole tumor to reach temperature over $45°C$ and the over-heating volume may be different in each case. Figure 21 (a) shows that it takes 11.5 minutes to make the whole tumor to reach a temperature over $45°C$ and the over-heating volume is $11.03\,cm^3$; Figure 21 (b) shows that it takes 9.5 minutes to cause the whole tumor to have a temperature over $45°C$ and the over-heating volume is $12.84\,cm^3$; Figure 21 (c) shows that it takes 8 minutes to make the whole tumor temperature over $45°C$ and the over-heating volume is $13.95\,cm^3$. According to these simulated results, we can

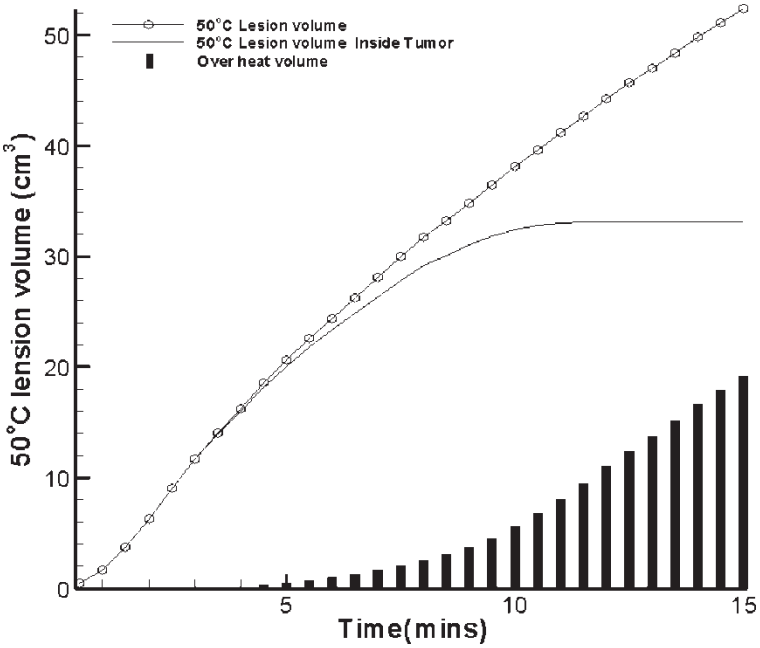

Figure 20. The simulated over-heating volumes that have reached 50°C in the tumor.

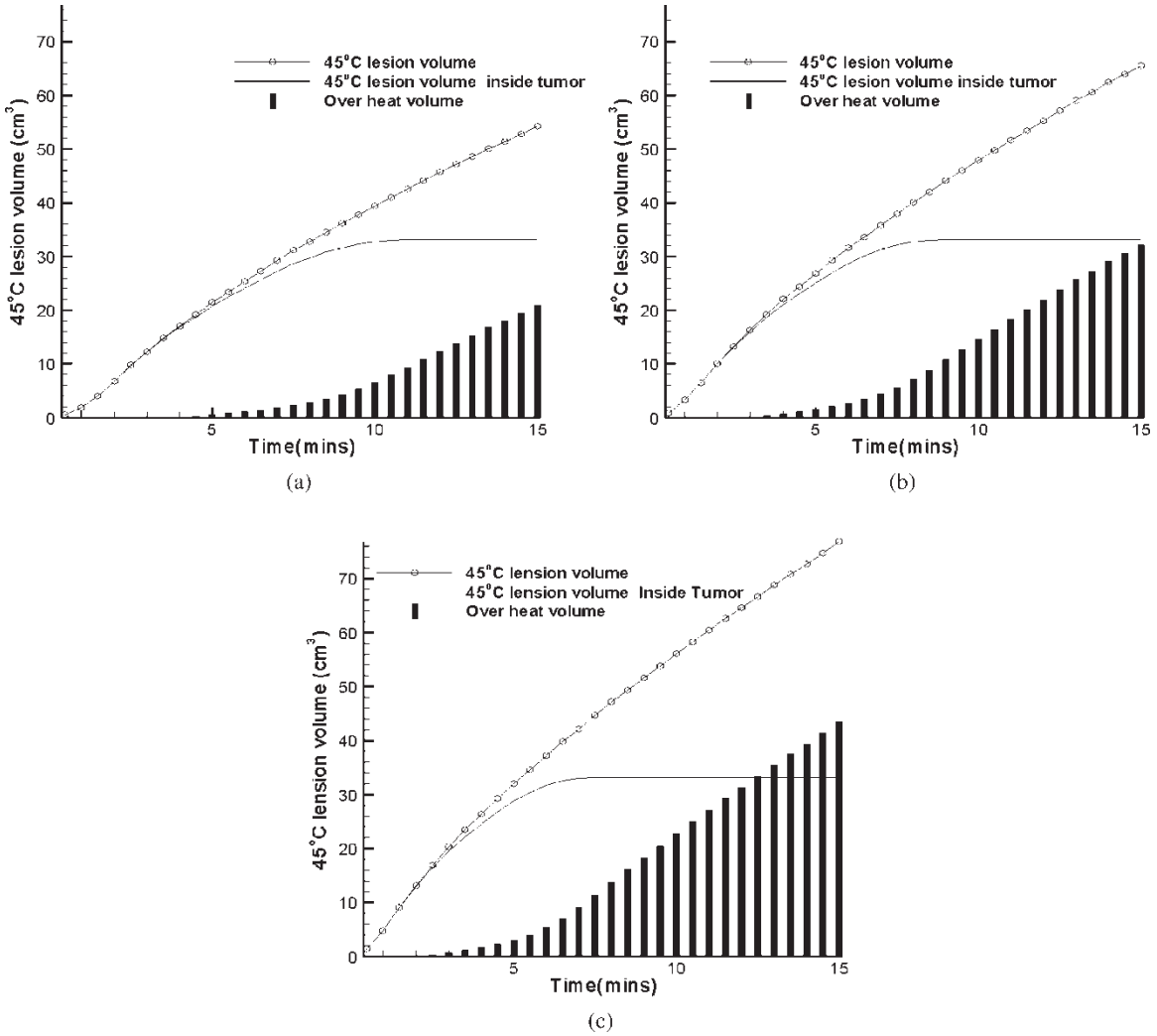

Figure 21. The simulated over-heating volumes that have reached 45°C in the tumor (a) 20 V; (b) 22.5 V; (c) 25 V.

conclude that the lower the applied voltage the longer the time is needed to destroy the whole tumor.

6. Conclusion

For accurately predicting the lesion area and decreasing the recurrence rate, we take the heat sink effect (or the liver perfusion) into account in the current finite volume RFA simulation. The study performed at the temperature controlled mode for a duration of 15 min is aimed to know better about the Joule heat deposited in the presence of liver vessel. We address in this study the heat that will be taken away from the blood vessel. To achieve the above goal, the heat transfer equation governing the emitted thermal energy generation from the electric current flowing through the investigated electrode will be solved during the hepatic ablation. Inclusion of Joule heat to the bioheat equation makes the modeling of heat transfer in liver tissues to be coupled with the electric field for the electric field intensity and current density. This thermo-electric system will be further complicated with the heat removal (or $h_{bl}(T-T_{bl})$) to account for the blood perfusion from the liver artery. The demand for a specification of convective heat transfer coefficient makes the investigated thermoelectric differential system even difficult to be tackled since it should be solved together with the flow equations, resulting in an electric–thermal–hydro-dynamic three-field coupling system for the RFA model.

Acknowledgements

This work is sponsored by National Science Council under NS C92-2218-E-002-026-Y. F. The author would like to thank Dr C. M. Chen in Tungs' Taichung Metro Habor Hospital for his provision of useful medical knowledge.

References

H. Arkin, L.X. Xu and K.R. Holmes, "Recent developments in modeling heat transfer in blood perfused tissues", *IEEE Trans. Biomed. Eng.*, 41, pp. 97–107, Feb 1994.

Isaac Chang, "Finite-element analysis of hepatic radio-frequency ablation probes using temperature-dependment electrical conductivity", *BioMed. Eng. OnLine*, May 2003.

S.A. Curley, F. Izzo, P. Delrio, L.M. Ellis, J. Granchi, P. Vallone, F. Fiore, S. Pignata, B. Banielle and F. Cremona, "Radiofrequency ablation of unresectable primary and metastatic hepatic malignancies: Results in 123 patients", *Ann. Surg.*, 230, pp. 1–8, 1999.

S.A. Curley, F. Izzo, L.M. Ellis, J.N. Vauthey and P. Vallone, "Radiofrequency ablation of hepatocellular cancer in 110 patients with cirrhosis", *Ann. Surg.*, 232, pp. 381–391, 2000.

E.S. Ebbini, S.I. Umemura, M. Ibbini and C.A. Cain, "A cylindrical-section ultrasound phased-array applicator for hyperthermia cancer therapy", *IEEE Trans. Biomed. Eng.*, 35, pp. 561–572, Sept 1988.

G.S. Gazelle, S.N. Goldberg, L. Solbiati and T. Livoraghi, "Tumor ablation with radio-frequency Energy", *Radiology*, 217(3), pp. 633–646, 2000, December 1.

S.N. Goldberg, G.S. Gazelle, C.C. Compton and T.C. McLoud, "Radiofrequency tissue ablation in the rabbit lung: efficacy and complications", *Acad. Radial.*, 48(2), pp. 776–784, 1995.

D. Haemmerich, S. Tyler Staelin, Supan Tungjitkusolmun, Fred T. Lee, Jr, David M. Mahvi and John G. Webster, "Hepatic bipolar radiofrequency ablation between separated multiprong electrodes", *IEEE Trans. Biomed. Eng.*, 48(10), October 2001.

J.S. Huang, D.A. Gervais and P.R. Mueller, "Radiofrequency ablation: Review of mechanism, indications, technique, and results", *Chin. J. Radiol.*, 26, pp. 119–134, 2001.

S.M. Lin and D.Y. Lin, "Percutaneous local ablation therapy in small hepatocellular carcinoma", *Chang. Gung. Med. J.*, 26(5), pp. 308–313, 2003.

T. Lorentzen, "A cooled needle electrode for radiofrequency tissue ablation: thermodynamic aspects of improved performance compared with conventional needle design", *Acad. Radiol.*, 3, pp. 556–563, 1996.

J.P. McGaham, P.D. Browning, J.M. Brock and H. Tesluk, "Hepatic ablation using radiofrequency electrocautery", *Invest. Radiol.*, 25, pp. 267–270, 1990.

J.D. McGaham, J.M. Brock, H. Tesluk, W.Z. Gu, P. Schneider and P.D. Browing, "Hepatic ablation with use of radio-frequency dectrocautery in the animal model", *J. Vasc. Inter. Radiol.*, 3, pp. 291–297, 1992.

S. Nath, J.P. DiMarco and D.E. Haines, "Basic aspects of radiofrequency catheter ablation", *J. Cardiovasc. Electrophysiol.*, 5, pp. 863–876, 1994.

RadioTherapeutics, Radiofrequency Ablation System, 2002. http://www.radiotherapeutics.com/physicians.shtml

Radionics, Cool-Tip RF Ablation, 2002. http://www.radionics.com/products/ablation/cooltip.shtml

Rita Medical Systems, Starburst XL needle, 2002. http://www.ritamedical.com/products.shtml

D.I. Rosenthal, A. Alexander, A.E. Rosenberg and D. Winfield, "Ablation of osteoid osteomas with a percutaneously placed electrode: a new procedure", *Radiology*, 183, pp. 29–33, 1992.

G. Steele and T.S. Ravikumar, "Resection of hepatic mestastases from colorectal cancer", *Ann. Surg.*, 210, pp. 127–138, 1989.

The Liver Cancer Study Group of Japan, "Primary liver cancer in Japan", *Cancer*, 60, pp. 1400–1411, 1987.

Supan Tungjitkusolmun, S. Tyler Staelin, Dieter Haemmerich, Jang-Zern Tsai, Hong Cao and JohnG. Webster, "Three-dimensional finite-element analysis for radio-frequency hepatic tumor ablation between", *IEEE Trans. Biomed. Eng.*, 49(1), 2002.